


Article

# Ablation Behavior of the SiC-Coated Three-Dimensional Highly Thermal Conductive Mesophase-Pitch-Based Carbon-Fiber-Reinforced Carbon Matrix Composite under Plasma Flame

Chong Ye <sup>1,2</sup>, Dong Huang <sup>1,2,\*</sup>, Baoliu Li <sup>1</sup>, Pingjun Yang <sup>1</sup>, Jinshui Liu <sup>1</sup>, Huang Wu <sup>1,2</sup>, Jianxiao Yang <sup>1</sup>  and Xuanke Li <sup>1,3,\*</sup>

<sup>1</sup> College of Materials Science and Engineering, Hunan Province Key Laboratory for Advanced Carbon Materials and Applied Technology, Hunan University, Changsha 410082, China

<sup>2</sup> Hunan Province Engineering Research Center for High Performance Pitch Based Carbon Fiber, Hunan Toyi Carbon Material Technology Co., Ltd., Changsha 410000, China

<sup>3</sup> The State Key Laboratory of Refractories and Metallurgy, Wuhan University of Science and Technology, Wuhan 430081, China

\* Correspondence: hd52923212@hnu.edu.cn (D.H.); xuankeli@hnu.edu.cn (X.L.); Tel./Fax: +86-0731-89729217 (D.H.)

Received: 7 July 2019; Accepted: 22 August 2019; Published: 25 August 2019



**Abstract:** This study is focused on a novel high-thermal-conductive C/C composite used in heat-redistribution thermal protection systems. The 3D mesophase pitch-based carbon fiber (CF<sub>MP</sub>) preform was prepared using CF<sub>MP</sub> in the X (Y) direction and polyacrylonitrile carbon fiber (CF<sub>PAN</sub>) in the Z direction. After the preform was densified by chemical vapor infiltration (CVI) and polymer infiltration and pyrolysis (PIP), the 3D high-thermal-conductive C/C (C<sub>MP</sub>/C) composite was obtained. The prepared C<sub>MP</sub>/C composite has higher thermal conduction in the X and Y directions. After an ablation test, the CF<sub>PAN</sub> becomes needle-shaped, while the CF<sub>MP</sub> shows a wedge shape. The fiber/matrix and matrix/matrix interfaces are preferentially oxidized and damaged during ablation. After being coated by SiC coating, the thermal conductivity plays a significant role in decreasing the hot-side temperature and protecting the SiC coating from erosion by flame. The SiC-coated C<sub>MP</sub>/C composite has better ablation resistance than the SiC-coated C<sub>PAN</sub>/C composite. The mass ablation rate of the sample is 0.19 mg·(cm<sup>-2</sup>·s<sup>-1</sup>), and the linear ablation rate is 0.52 μm·s<sup>-1</sup>.

**Keywords:** carbon–carbon composites; ablation; high-temperature properties; microstructure

## 1. Introduction

Carbon-fiber-reinforced carbon matrix (C/C) composite has been widely studied due to its high-temperature strength, low coefficient of thermal expansion, and good anti-ablation ability [1,2]. Because of its excellent performance, C/C composite has become a promising structural material in high-temperature applications, including rocket nozzles, aeronautic jet engines, leading edges, and so on. C/C composite is also a promising functional material for thermal management systems due to its high thermal conductivity [3,4]. Because it can decrease the temperature of hot components and consequently increase their reliability, C/C composite has been used in heat-redistribution thermal-protection systems of hypersonic aircraft that have undergone long-time ablation and oxidation [5].

There have been many studies on the effects of voids, carbon fibers, and matrix and the interfaces between them on the mechanical and thermal performance of C/C composites. Lachaud et al. [6] set up a modeling strategy to predict 3D C/C composite ablation behavior, and the models were consistent with

the experimental data. Lee et al. [7] characterized the surface microstructure of a 2D  $C_{PAN}/C$  composite and found that the transverse  $CF_{PAN}$  of flank surface had a random orientation of basal planes that was different from the fiber surface. Baxter et al. [8] studied the effect of chemical vapor infiltration (CVI) on the corrosion and thermal conduction of porous  $C/C$  composite, and found that both radiative heat transfer and the heat transfer path in pores played important roles in the parallel path thermal conduction. The ablation behavior of  $C/C$  composite was also studied by other researchers [9,10]. As for high-thermal-conductive  $C/C$  composite, carbon fiber (CF) is not only the reinforcement of the composite, but also the carrier of heat [11]. The morphology, crystal orientation, and crystallite structure of the carbon fiber have an obvious influence on the heat transfer of  $C/C$  composite [12,13]. Polyacrylonitrile (PAN)-based and pitch-based carbon fibers are the most common carbon fibers [14,15]. In comparison with PAN-based carbon fiber ( $CF_{PAN}$ ), mesophase pitch-based carbon fiber ( $CF_{MP}$ ) has higher thermal conductivity due to fewer lattice defects, higher preferred orientation, and larger graphite crystallite size [15,16]. Therefore,  $CF_{MP}$  is an ideal reinforcement for  $C_{MP}/C$  composite with high thermal conductivity. Many studies have focused on developing high-thermal-conductive  $C_{MP}/C$  composites. Yuan et al. [17] prepared a 1D ribbon-shaped carbon-fiber-reinforced  $C_{MP}/C$  composite, and the longitudinal thermal conductivity was about  $900 \text{ W}\cdot(\text{m}^{-1} \text{ K}^{-1})$  after graphitization. Adams et al. [18] and Manocha et al. [4] analyzed the microstructure and thermophysical properties of  $C_{MP}/C$  composite. Although much data has been reported in the literature on the fabrication of high-thermal-conductive  $C_{MP}/C$  composite [18] and there has been evaluation of the thermophysical properties [19,20] and analysis of the thermal conductivity mechanism [21,22], there have been few reports on the ablation behavior of  $C_{MP}/C$  composite, which is worth exploring. It is known that the microstructures and properties of  $CF_{MP}$  and  $CF_{PAN}$  are evidently different. High-thermal-conductive  $CF_{MP}$  has been proven to have a perfect graphite crystal structure highly oriented along the fiber axis direction, while  $CF_{PAN}$  exhibits a turbostratic structure composed of entangled and wrinkled crystallites [13,16]. Therefore, it can be speculated that  $C_{MP}/C$  composite using  $CF_{MP}$  as reinforcement will have some different ablation features. Such understanding of the ablation behavior of  $C_{MP}/C$  composite is helpful in applying this composite to thermal protection systems of hypersonic vehicles, especially in explaining the failure mechanisms after the thermal protection coating is damaged. In addition, poor oxidation resistance of carbon materials (above  $500 \text{ }^\circ\text{C}$ ) has greatly restricted the application of  $C_{MP}/C$  composite under high-temperature environments. Therefore, a thermal protective coating is also needed to make the high thermal conductivity play its positive role in ablation [23,24]. All of this should be experimentally investigated.

In this paper, we report the ablation behavior of a novel homemade 3D  $C_{MP}/C$  composite with high thermal conductivity. The  $C_{MP}/C$  composite was prepared using  $CF_{MP}$  as the reinforcement and heat carrier in the X (Y) direction and  $CF_{PAN}$  in the Z direction. The influence of thermal diffusion and structure on the ablation behavior of  $C_{MP}/C$  composite with and without SiC coating is elucidated. This study can provide guidance for the design and fabrication of  $C_{MP}/C$  composite with high thermal conductivity for application in hypersonic aircrafts.

## 2. Experimental Procedures

### 2.1. Material Preparation

The high-thermal-conductive  $C_{MP}/C$  composite was prepared as follows (Figure 1a).

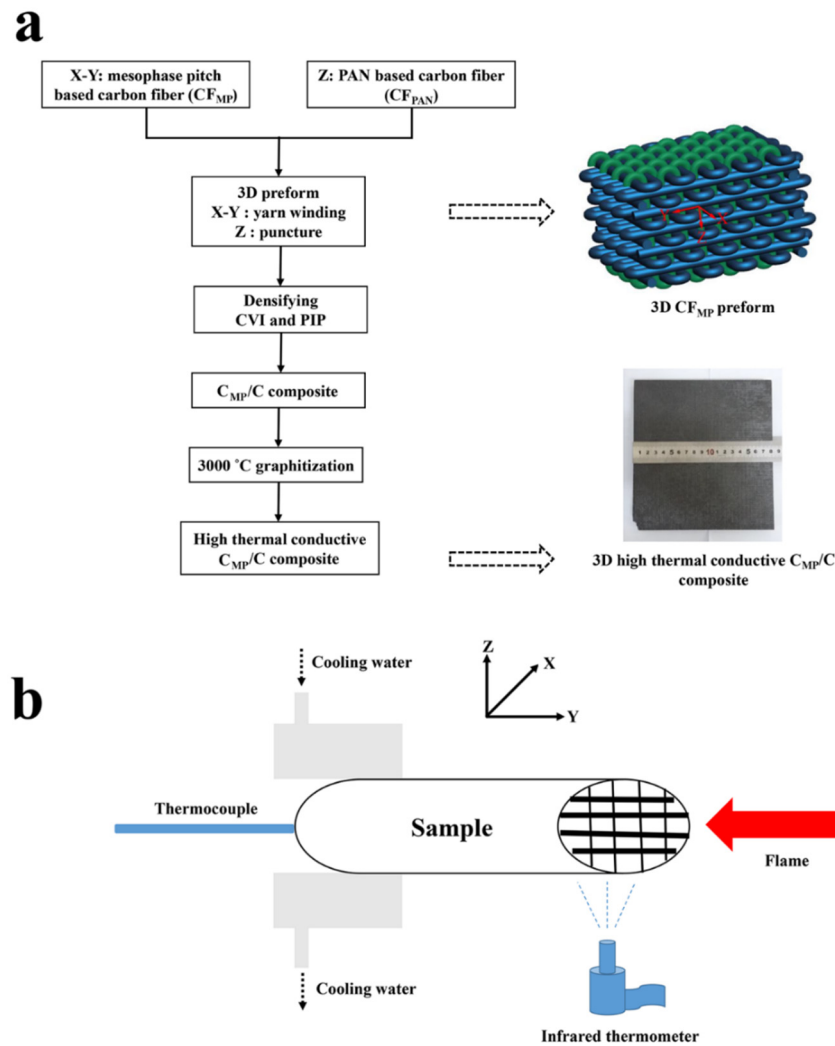


**Figure 1.** (a) Preparation process and (b) ablation test of  $C_{MP}/C$  composite. CVI, chemical vapor infiltration; PIP, polymer infiltration and pyrolysis;  $C_{MP}$ , mesophase pitch-based carbon fiber.

First, homemade  $CF_{MP}$  (Hunan University, Changsha, China) was used as a reinforcement and heat carrier of the composites in both X and Y directions by yarn winding, and commercially available  $CF_{PAN}$  (T700, Toray, Tokyo, Japan) was used as the reinforcement in the Z direction by puncture in order to improve the mechanical properties of the composite (Figure 1). Table 1 shows the characteristics of the carbon fibers in the  $C_{MP}/C$  and  $C_{PAN}/C$  composites. The density of the preform is roughly  $0.9 \text{ g}\cdot\text{cm}^{-3}$ .

**Table 1.** Characteristics of carbon fiber in  $C_{MP}/C$  composite.  $CF_{MP}$ , mesophase pitch-based carbon fiber;  $CF_{PAN}$ , polyacrylonitrile carbon fiber.

	Thermal Conductivity ( $\text{W}\cdot\text{m}^{-1}\cdot\text{K}^{-1}$ )	Volume Fraction (%)	Direction
$CF_{MP}$	$\geq 700$	36	X, Y
$CF_{PAN}$	$\sim 10$	8–10	Z

Second, 3D  $CF_{MP}$  preform filling or densification was accomplished by a combination of chemical vapor infiltration (CVI) and polymer infiltration and pyrolysis (PIP). CVI densification was performed in a hot-wall furnace, and the pressure was 3.0 kPa. The reaction was at  $950 \text{ }^\circ\text{C}$  using  $\text{C}_3\text{H}_6$  as the carbon precursor gas and nitrogen as the carrier gas at a volumetric ratio of 2:5. The density of the sample was about  $1.6 \text{ g}\cdot\text{cm}^{-3}$  after CVI for 80 h. Subsequently, the impregnation and solidification

processes were repeated 4–6 times using furan resin as the precursor. Then, carbonization was carried out in the furnace at 900 °C in a nitrogen atmosphere. After PIP and CVI, pyrolytic carbon (PyC) was formed into the preform and wrapped around the carbon fibers. The 3D C<sub>PAN</sub>/C composite using CF<sub>PAN</sub> as reinforcement in all directions was prepared by the same method and was used as the control.

Finally, after graphitization at 3000 °C under an argon atmosphere, the 3D high-thermal-conductive C<sub>MP</sub>/C composite and low-thermal-conductive C<sub>PAN</sub>/C composite with a density of 1.82–1.84 g/cm<sup>3</sup> were obtained.

The SiC coating was fabricated on the surface of the samples by the same chemical vapor reaction (CVR) to develop ablation resistance. Then, the C<sub>MP</sub>/C and C<sub>PAN</sub>/C composites were ground with SiC papers (800 grit), ultrasonically cleaned and dried, and the SiC coating was fabricated on the composites by the CVR process. The SiO<sub>2</sub>/Si mixture was heated at 1500–1800 °C to produce SiO gas. The CVR SiC coating was prepared by a reaction between the SiO gas and the C<sub>MP</sub>/C or C<sub>PAN</sub>/C composite at 2200 °C in a graphite furnace, to obtain SiC-coated samples.

## 2.2. Ablation and Oxidation Tests

The ablation resistance of the C<sub>MP</sub>/C and C<sub>PAN</sub>/C composite samples (Ø5 × 35 mm) was tested by water plasma equipment (Multiplaz 3500, muzzle inner diameter 3–5 mm). The ablation direction of the flame was parallel to the X (Y) direction of the preform (Figure 1). The distance between the muzzle and the composite was 10 mm, and the composite was ablated for 120 s. The maximum temperature of the plasma was about 2300 °C, as measured by an optical pyrometer. The surface temperature (hot side) of the specimen was monitored by a noncontact infrared pyrometer, while the back temperature (cool side) was measured by the thermocouple. The average ablation rates were calculated using five samples. The mass ablation rate was calculated using Equation (1):

$$R_m = \Delta m \cdot S^{-1} \cdot t^{-1} \quad (1)$$

where  $R_m$  is the mass ablation rate (mg·cm<sup>-2</sup>·s<sup>-1</sup>),  $\Delta m$  is the mass change of the sample (mg),  $S$  is the surface area of the coating (cm<sup>2</sup>), and  $t$  is the ablation time (s).

The linear ablation rate was calculated by Equation (2):

$$R_l = \Delta l \cdot t^{-1} \quad (2)$$

where  $R_l$  is the linear ablation rate (µm·s<sup>-1</sup>),  $\Delta l$  is the length change of the sample (µm), and  $t$  is the ablation time (s).

The static oxidation behavior of the samples was tested in a muffle furnace. After being heated to 1500 °C for 10 min in the furnace, the samples cooled down to room temperature. Air was used as the oxidizing gas in the furnace, and the cooling rate was 100 °C·min<sup>-1</sup>.

## 2.3. Material Characterization

The structure and morphology of the samples were analyzed by scanning electron microscopy (SEM; FEI Nova Nano SEM230, Hillsboro, OR, USA), and the phase composition of the samples was characterized by X-ray diffraction (XRD; Rigaku Dmax 2550VB + 18 KW, Tokyo, Japan).

The thermal conductivity of the carbon fibers was obtained by an indirect test method. After measuring the axial electrical resistivity of the carbon fibers with the four-probe method, the thermal conductivity values were calculated using Equation (3):

$$\lambda = 1261/\rho \quad (3)$$

where  $\lambda$  is the thermal conductivity and  $\rho$  is the specific resistance.

The thermal diffusivity of the composites was tested by a laser flash diffusivity apparatus (NETZSCH, Selb, Germany). The thermal conductivity was calculated using Equation (4):

$$k = \alpha \cdot c_p \cdot \rho \quad (4)$$

where  $\alpha$  is the thermal diffusion coefficient,  $c_p$  is the specific heat at constant pressure, and  $\rho$  is density.

### 3. Results and Discussion

#### 3.1. Microstructure of the Composites

The room-temperature thermal diffusion of the  $C_{MP}/C$  composite is closely related to the composition, structure, and arrangement orientation of the carbon fibers and carbon matrix. The room-temperature thermal conductivity of the homemade  $C_{MP}/C$  and  $C_{PAN}/C$  composites is shown in Figure 2. It is known that the orientation and size of the graphite layer play important roles in the thermal conductivity of carbon fibers. The homemade  $CF_{MP}$  had a larger graphite crystallite size, higher preferred orientation degree along the axis, and fewer crystallite defects, so it had higher thermal conductivity than  $CF_{PAN}$ . The thermal conductivity of  $CF_{MP}$  and the  $CF_{PAN}$  is about  $700 \text{ W}\cdot\text{m}^{-1}\cdot\text{K}^{-1}$  and  $10 \text{ W}\cdot\text{m}^{-1}\cdot\text{K}^{-1}$ , respectively (Table 1). Figure 2 shows that the thermal conductivity of the  $C_{MP}/C$  composite ( $218.2 \text{ W}\cdot\text{m}^{-1}\cdot\text{K}^{-1}$ ) is evidently higher in the X and Y directions than that of the  $C_{PAN}/C$  composite ( $36.1 \text{ W}\cdot\text{m}^{-1}\cdot\text{K}^{-1}$ ). It is speculated that the  $C_{MP}/C$  composite can transfer heat from the hot side to the cool side more efficiently than the  $C_{PAN}/C$  during ablation in the X or Y direction. In addition, because  $CF_{MP}$  in the X (Y) direction has higher thermal conductivity and a higher volume fraction than  $CF_{PAN}$  in the Z direction (Table 1), the thermal conductivity of the  $C_{MP}/C$  composite in the X (Y) direction is higher than that in the Z direction.

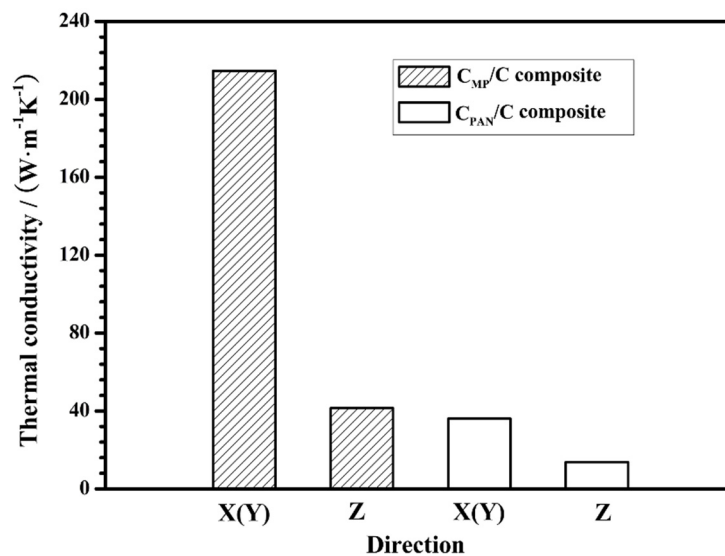


**Figure 2.** Thermal conductivity of  $C_{MP}/C$  and  $C_{PAN}/C$  composites.  $C_{PAN}$ , polyacrylonitrile (PAN)-based carbon fiber.

Figure 3 shows the microstructure of the  $C_{MP}/C$  composite. It can be seen that the  $C_{MP}/C$  composite contains a small amount of cracks, voids, and debonded fiber/matrix interfaces. However, the composite is almost compact after densification (Figure 3a). Figure 3b shows that the round-shaped  $CF_{PAN}$  in the Z direction is coated with PyC. The thickness of the PyC layer in  $CF_{PAN}$  is less than that of the  $CF_{MP}$  due to smaller gaps in  $CF_{PAN}$ . The arrows in Figure 3a,c indicate the direction of the  $CF_{MP}$  bundle in the composite. Compared to  $CF_{PAN}$ , with thermal conductivity of about  $10 \text{ W}\cdot\text{m}^{-1}\cdot\text{K}^{-1}$ , it is evident that  $CF_{MP}$  has higher thermal conductivity, reaching to above  $700 \text{ W}\cdot\text{m}^{-1}\cdot\text{K}^{-1}$ , which can contribute to the highly oriented graphitic structure along the fiber axis, larger crystal size, and more

perfect crystallinity of  $CF_{MP}$  [13]. Thus, the  $C_{MP}/C$  composite has higher thermal conductivity in the X (Y) direction. High-magnification images indicate good interface bonding between PyC and  $CF_{MP}$ , and resin carbon can also be found in the gaps among the PyC layers.

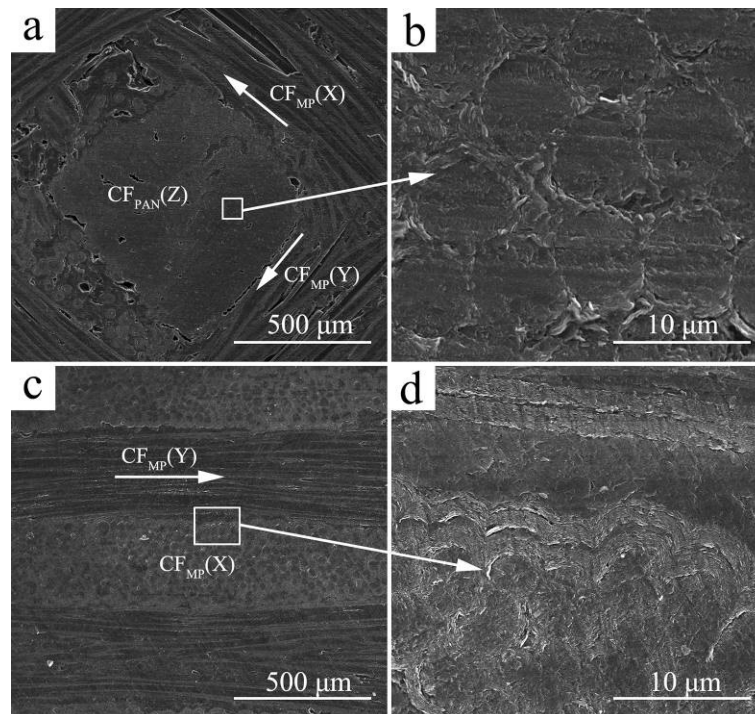


**Figure 3.** Microstructure of  $C_{MP}/C$  composite: (a) X–Y plane; (b)  $CF_{PAN}$  in the Z direction; (c) Y–Z plane; (d) high-magnification image.

To further understand the influence of the microstructure of  $C_{MP}/C$  composite on its ablation behavior, its fracture morphology was investigated (as shown in Figure 4). The location of this particular fracture in Figure 4 refers to the region of the dashed white lines in Figure 3c. Carbon fiber pull-out and interface debonding can be observed after rupture failure of the  $C_{MP}/C$  composite (Figure 4a). It is interesting to find that the open wedge crack texture of the round-shaped  $CF_{MP}$  is observed in the  $C_{MP}/C$  composite (Figure 4b). It is reported that the linear domain units in  $CF_{MP}$  induced circumferential shrinkage at the spinning and further heat-treatment steps, leading to the formation of the open crack [13,25]. Figure 4c indicates that  $CF_{MP}$  is composed of a highly graphitic flat-layered structure radially oriented in the transverse section. The thermal conductivity of the carbon materials can be calculated according to the following formula:

$$\lambda = 1/3CvL \quad (5)$$

where  $\lambda$  is the thermal conductivity,  $v$  is the propagation velocity of the phonon, and  $L$  is the free path of the phonon.  $CF_{MP}$  has well-developed graphene sheets and a highly preferentially oriented crystal structure along the longitudinal and radial directions, which can provide fast thermal diffusion in phonon heat conduction. After graphitization, the layered structure of PyC is also formed (Figure 4d). Because the diameter of  $CF_{MP}$  is larger and the gas precursor has a larger diffusion space in the preform during the CVI process, the PyC layer around  $CF_{MP}$  is thicker than that around  $CF_{PAN}$ .

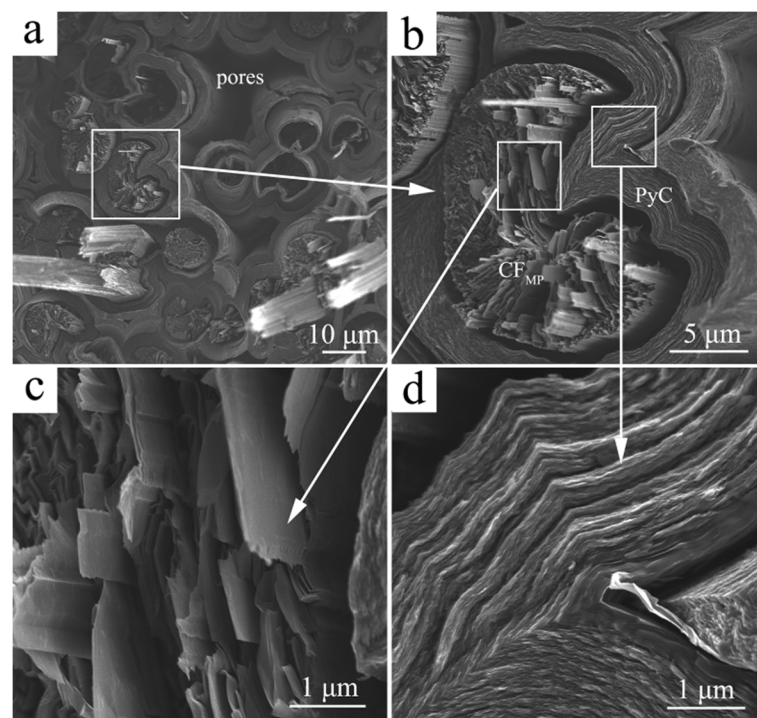


**Figure 4.** SEM images of fracture section of  $C_{MP}/C$  composite: (a) low-magnification image; (b–d) high-magnification images of PyC-coated  $CF_{MP}$ , highly preferentially oriented crystal structure in  $CF_{MP}$  (c) and PyC (d). The white arrows show the regions at high magnification.

### 3.2. Ablation Behavior of $C_{MP}/C$ Composite

Figure 5 shows SEM images of the  $C_{MP}/C$  composite (X–Z plane) after ablation. The ablated surface exhibits a rough and porous morphology and is mainly composed of ablated carbon fiber and matrix. It can be seen that both  $CF_{MP}$  in the X (Y) direction and  $CF_{PAN}$  in the Z direction are ablated (Figure 5a), but they show different ablation characteristics.  $CF_{PAN}$  becomes needle-shaped after ablation (Figure 5b), which has been reported by many studies [24–26]. Because  $CF_{PAN}$  has a turbostratic structure with physical entanglements and covalent cross-links, its cross-section after ablation looks like a homogeneous structure (Figure 5c) [15,16]. No peeling of the graphene sheet is observed. Compared to  $CF_{PAN}$ ,  $CF_{MP}$  shows a wedge shape after ablation (Figure 5d). The layered structure in the fiber axis direction is formed after ablation, as shown in Figure 5e, suggesting that the mass loss preferentially takes place at the edges of layers or among layers because of the radial texture of  $CF_{MP}$ . Figure 5f exhibits the ablated morphology of  $CF_{MP}$  in the X direction, showing that the matrix (PyC) around the fiber bundles is eroded and forms a shell shape, and then is stripped off by the plasma flame. Before ablation, the boundary inside the carbon matrices and the CF/PyC interface presents good compatibility, and there is no PyC matrix microcracking or obvious interfacial debonding (Figure 3d). However, after ablation, many gaps or cracks are formed in the PyC matrix, the CF bundle, and the interface between them (Figure 5h). These indicate that ablation and oxidation begin at the CF/PyC interface and the boundary inside the PyC matrix, which are much easier to oxidize than the PyC matrix because of the more active sites in carbon nets. It is noted that many ablated defects, such as gaps or cracks, are also formed in the radial direction of  $CF_{MP}$  (Figure 5g).

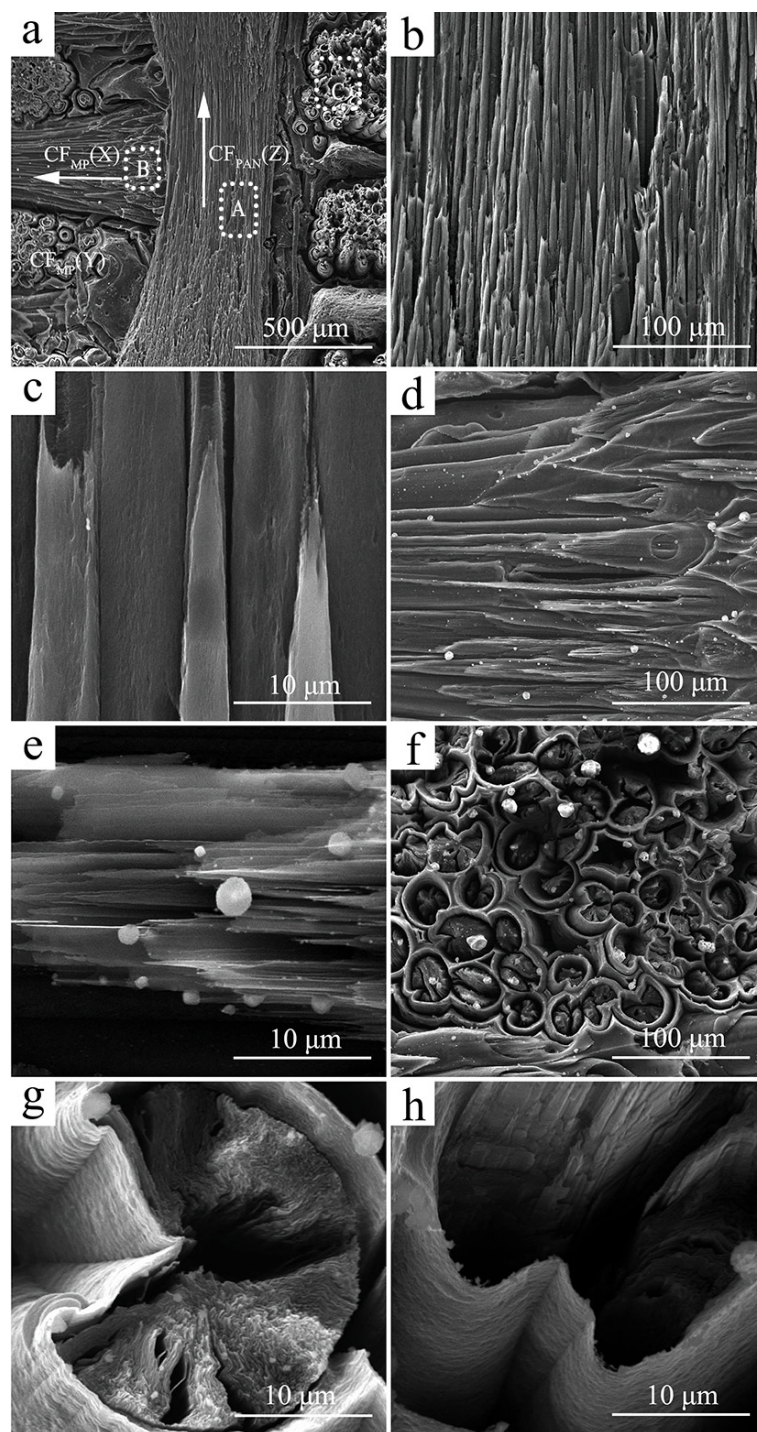


**Figure 5.** SEM images of  $C_{MP}/C$  composite after ablation: (a) microstructure in the ablation center; (b) low-magnification image of  $CF_{PAN}$  in the Z direction (region A in (a)); (c) high-magnification image of  $CF_{PAN}$  in the Z direction (region A in (a)); (d) low-magnification image of  $CF_{MP}$  in the Y direction (region B in (a)); (e) high-magnification image of  $CF_{MP}$  in the Y direction (region B in (a)); (f) low-magnification image of  $CF_{MP}$  in the X direction (region C in (a)); (g) high-magnification image of  $CF_{MP}$  in the X direction (region C in (a)); (h) interface between PyC layers after ablation (region C in (a)). The white arrows in (a) show the directions of the  $CF_{PAN}$  and  $CF_{MP}$ .

In order to better analyze the ablation behavior of  $C_{MP}/C$  composite, we performed an oxidation test (Figure 6). It is observed that oxidation preferentially occurs at the CF/PyC interface, which is similar to ablation. When oxygen diffuses from the outer to the inner part of the  $C_{MP}/C$  composite,



the CF/PyC interface and boundary inside the matrix oxidize much more easily than the PyC matrix because there are more active sites in carbon nets (Figure 6a). The cross-section of CF<sub>MP</sub> after the oxidation test shows a more homogeneous morphology compared to the ablation test (shown in Figure 5g). Many small holes formed by oxidation can be observed in Figure 6b. The highly conductive CF<sub>MP</sub> in this study has a radial structure and weaker bonding among the highly oriented graphene layers. It can be speculated that the carbon atoms at these active sites may preferentially react with oxygen, leading to the radial carbon fragments formed by oxidation being easily stripped away from the CF<sub>MP</sub> (Figure 5g). Figure 6c shows the oxidation characteristics in the length direction of CF<sub>MP</sub>. Many slits are observed after oxidation, which can provide oxygen diffusion paths in the CF<sub>MP</sub> during oxidation. Figure 6d shows the oxidation characteristics in the carbon matrix. It can be seen that the PyC/PyC interface is more easily oxidized than the PyC itself. Slits are formed in the PyC/PyC interface, and some small holes are observed on the surface of the PyC matrix, indicating that the PyC/PyC interface presents higher chemical reactivity than the PyC matrix itself during oxidation. In addition, the oxidation and ablation tests showed that a thermal protective coating is necessary to prevent the C<sub>MP</sub>/C composite from being damaged in the oxygen atmosphere.

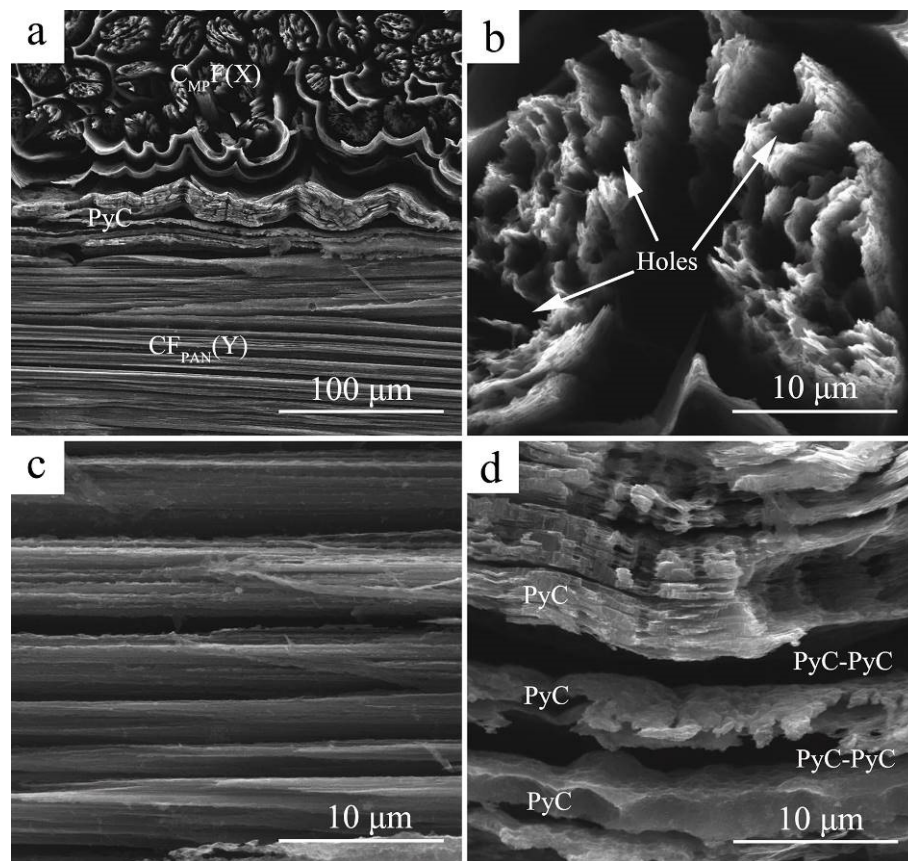


**Figure 6.** Microstructure of C<sub>MP</sub>/C composite after oxidation: (a) microstructure of the Y–Z plane; (b) CF<sub>MP</sub> in the X direction; (c) CF<sub>MP</sub> in the Y direction; (d) interface between PyC layers.

The ablation behavior of the C<sub>MP</sub>/C composite is mainly influenced by the oxidation reaction and the mechanical scouring caused by the plasma flame. The ablation behavior can be explained as follows (Figure 7): On the one hand, the oxidation reaction of the C<sub>MP</sub>/C composite refers to the heterogeneous reaction between the oxygen and the carbon phase, including carbon fiber and carbon matrix. The CF/PyC and PyC/PyC interfaces are preferentially oxidized and damaged due to the cracks and debonding defects. The PyC matrices around the CF bundle are burned into a shell shape, while the PyC matrices among the ablated CF are burned off. On the other hand, CF<sub>MP</sub> and

$CF_{PAN}$  exhibit different ablation behaviors due to their different structural characteristics.  $CF_{PAN}$ , with physical entanglements and covalent cross-links of turbostratic structure, becomes needle-shaped after ablation (Figure 5b). Compared to the homogeneous ablated structure of  $CF_{PAN}$ ,  $CF_{MP}$ —with a highly preferentially oriented crystal structure—shows a wedge shape after ablation. The carbon phases in or between the edges of the layers of the highly graphitic flat-layered structure are more easily oxidized and stripped away from the  $CF_{MP}$  during ablation. Therefore, the mass loss is observed in the radial direction.

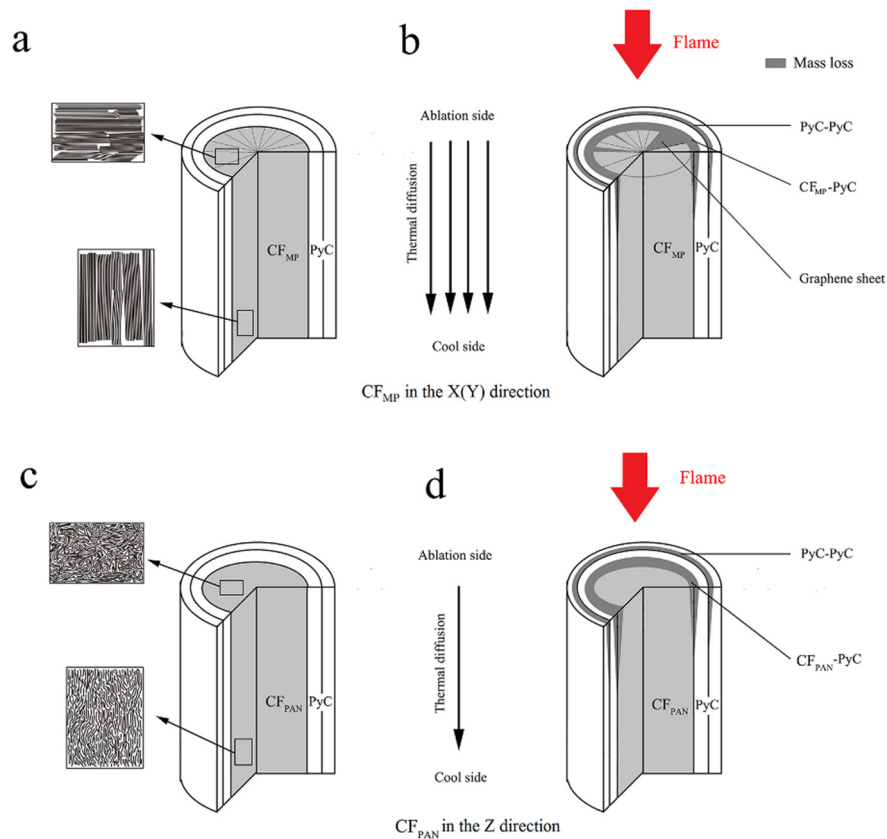


**Figure 7.** Ablation behavior of  $C_{MP}/C$  composite in different directions: (a)  $CF_{MP}$  in the X (Y) direction before ablation; (b)  $CF_{MP}$  in the X(Y) direction after ablation; (c)  $CF_{PAN}$  in the Z direction before ablation; (d)  $CF_{PAN}$  in the Z direction after ablation.

### 3.3. Ablation Behavior of SiC-Coated $C_{MP}/C$ Composite

In order to further optimize the ablation resistance of the  $C_{MP}/C$  composite, SiC coating was fabricated on the surface of samples by CVR (Figure 8). Figure 8b,c shows SEM images of the surface and cross-section of the coatings after CVR. The SiC coating surface seems to be coarse and rubble-like before ablation. The XRD pattern (Figure 8b) indicates that the coating is composed of  $\beta$ -SiC, which has three obvious characteristic peaks at  $35.7^\circ$ ,  $60.1^\circ$ , and  $71.8^\circ$  ((111), (220), and (311), respectively, in a Face-Centered Cubic lattice). Figure 8c shows that the thickness of the SiC coating is about 50–80  $\mu\text{m}$ , and there is no obvious crystal boundary in the cross-section (Figure 8c).

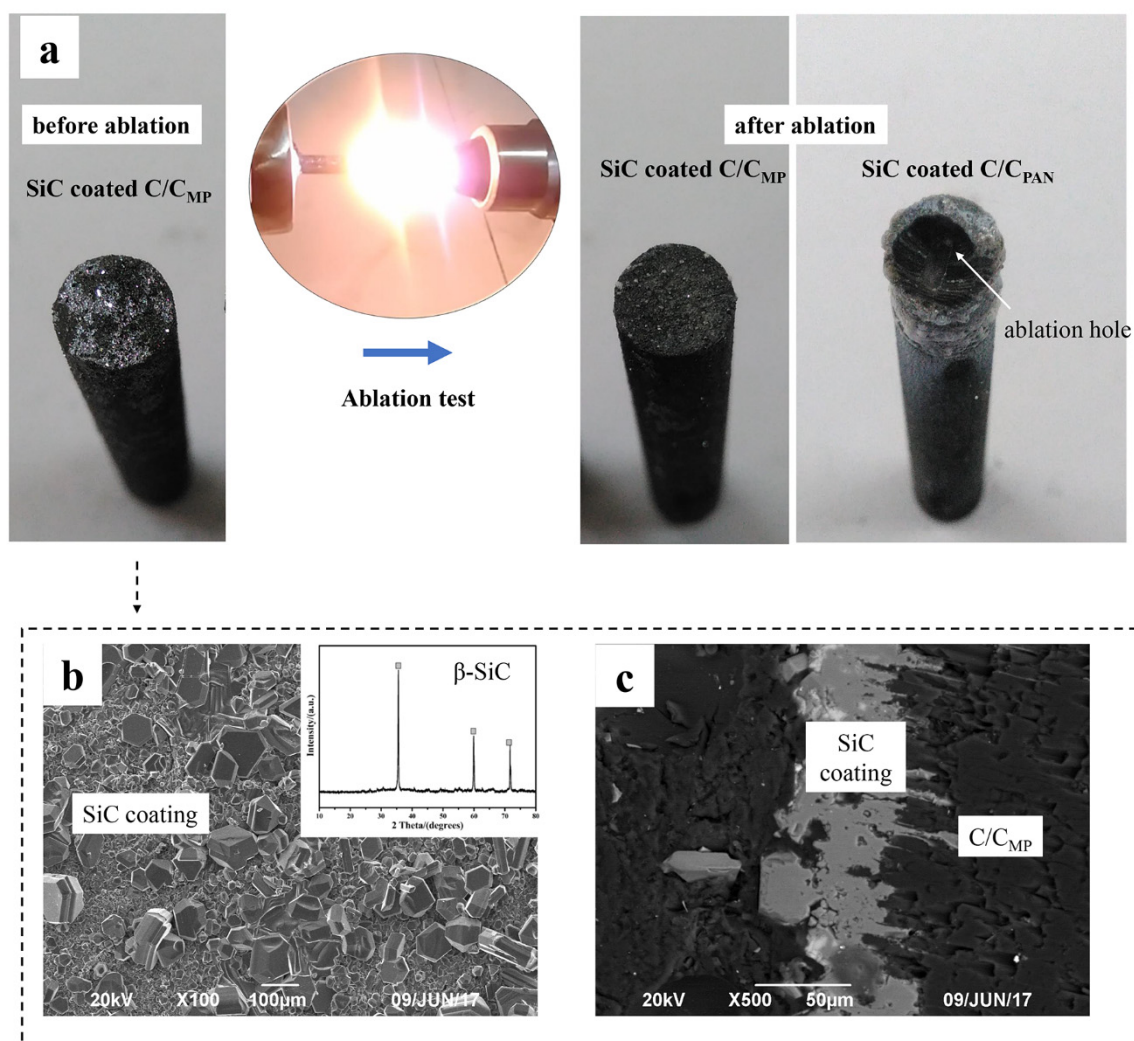


**Figure 8.** Microstructure of SiC coating: (a) photos of SiC-coated samples before and after ablation tests; (b) SEM image of the surface of the coating; (c) SEM image of the cross-section of the coating.

Photographs of the composites after 120 s of ablation are shown in Figure 9. The coating in the ablation center of C<sub>MP</sub>/C composite was not destroyed after ablation. The SiC grains were covered with a glass layer, which was identified as being SiO<sub>2</sub> by EDS results (Figure 9a). It is worth noting that the ablation temperature (2300 °C) exceeded the boiling point of SiO<sub>2</sub>, but the SiC was not evidently corroded during ablation; only a few pitting corrosion features were observed on the coating surface. In comparison, coating in the ablation center of C<sub>MP</sub>/C composite was stripped off and the carbon fibers were ablated. Although some ceramic oxide residues were observed on the surface, they could not prevent the carbon phase from erosion. Table 2 shows the ablation rates of the C<sub>PAN</sub>/C and C<sub>MP</sub>/C composites with and without SiC coating. It can be concluded that without SiC coating, both composites show similar ablation rates during the test because the carbon phases are more easily oxidized and then stripped from the composites. Thermal conductivity does not have an obvious effect on the thermal protection. However, the SiC-coated C<sub>MP</sub>/C composite shows better ablation resistance than the SiC-coated C<sub>PAN</sub>/C composite after a 120 s ablation test. The mass and linear ablation rates of the SiC-coated C<sub>PAN</sub>/C composite are 13.57 μm·s<sup>-1</sup> and 1.44 mg·(cm<sup>-2</sup>·s<sup>-1</sup>), respectively, and those of the SiC-coated C<sub>MP</sub>/C composite are only 0.52 μm·s<sup>-1</sup> and 0.19 mg·(cm<sup>-2</sup>·s<sup>-1</sup>), respectively. Thermal conductivity is believed to play a significant role in decreasing the hot-side temperature and protecting the SiC coating from corrosion by the flame.

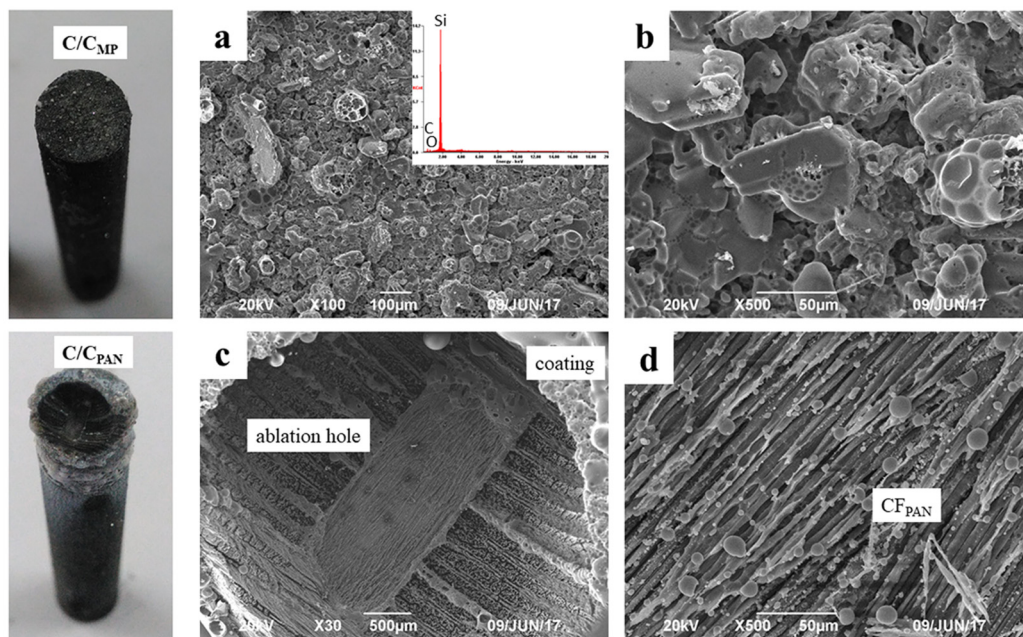


**Figure 9.** Microstructure of samples after ablation for 120 s: (a) low-magnification SEM image of ablation center on surface of SiC-coated  $C_{MP}/C$  composite; (b) high-magnification image of (a); (c) low-magnification SEM image of the ablation center on the surface of SiC-coated  $C_{PAN}/C$  composite; (d) high-magnification image of (c).

**Table 2.** Ablation rates of samples after ablation under air atmosphere for 120 s.

Sample	Linear Ablation Rate ( $\mu\text{m}\cdot\text{s}^{-1}$ )	Mass Ablation Rate ( $\text{mg}\cdot\text{cm}^{-2}\cdot\text{s}^{-1}$ )
SiC-coated $C_{MP}/C$	0.52	0.19
SiC-coated $C_{PAN}/C$	13.57	1.44
$C_{MP}/C$	28.21	12.24
$C_{PAN}/C$	26.45	11.31

Figure 10a shows the surface temperature curves of the  $C_{MP}/C$  and  $C_{PAN}/C$  composites. It shows that the thermal conductivity of the composite has an influence on its surface temperature, because the composite with higher thermal conductivity allows more heat to be conducted from heating zones (sample surface) to colder zones (sample back), and then be dissipated. It can be seen from Figure 10a that the surface temperature of the  $C_{MP}/C$  composite is about 1370 °C at 100 s, which is lower than the flame temperature (over 2300 °C) due to its high emissivity and thermal conductivity. The surface temperature of the  $C_{PAN}/C$  composite increases rapidly to about 1427 °C at 20 s, whereas that of the  $C_{MP}/C$  composite increases more slowly. After 100 s of ablation, the surface temperature of the  $C_{MP}/C$  composite is 149 °C lower than that of the  $C_{PAN}/C$  composite, indicating that  $CF_{MP}$  can effectively dissipate heat away from the hot side (ablation center) to the relatively cool side (sample back). It is believed that  $CF_{MP}$  is composed of a highly preferentially oriented crystal structure in the longitudinal direction, which can provide fast thermal diffusion in phonon heat conduction. The straight and continuous  $CF_{MP}$  can effectively decrease the surface temperature by rapidly transferring the heat to the back side, and then radiate the heat around the environment. Because the thermal conductivity of the  $C_{MP}/C$  composite ( $218.2 \text{ W}\cdot\text{m}^{-1}\cdot\text{K}^{-1}$ ) is much higher than that of the  $C_{PAN}/C$  composite ( $36.1 \text{ W}\cdot\text{m}^{-1}\cdot\text{K}^{-1}$ ) along the ablation direction (Figures 1 and 2), it can be concluded that more heat in the ablation center of the  $C_{MP}/C$  composite is dissipated away under the same conditions. Figure 10b shows that the temperature of the  $C_{MP}/C$  composite on the cool side (sample back) increases more than that of the  $C_{PAN}/C$  composite. At 100 s, the cool-side temperature of the  $C_{MP}/C$  composite is 20 °C higher than that of the  $C_{PAN}/C$  composite. The result also indicates that more heat can be

conducted from the ablation center (hot side) to the sample back (cool side) when  $C_{MP}$  with high conductivity is used in the composite. Based on this analysis, it can be concluded that the high conductivity of the  $C_{MP}/C$  composite ( $CF_{MP}$ ) plays a positive role in its ablation resistance.

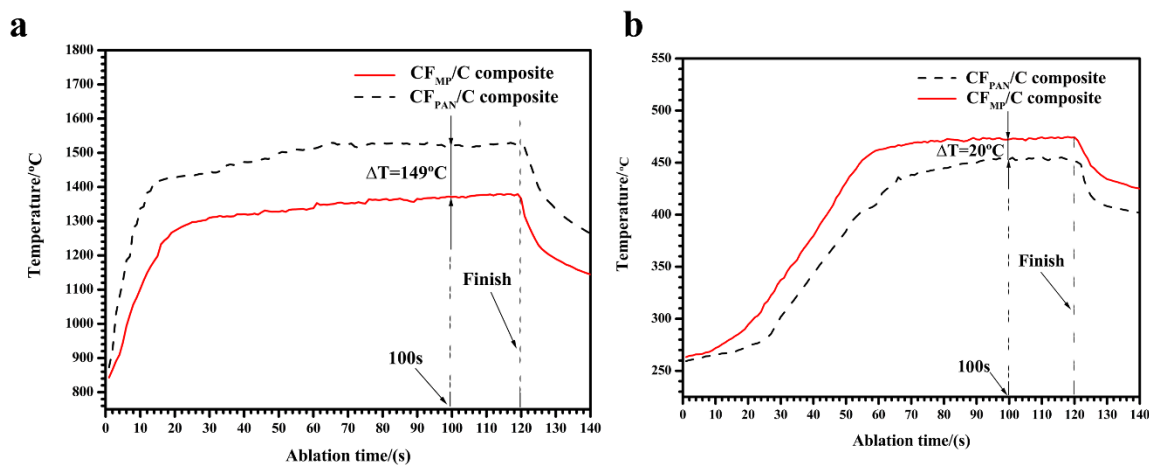


**Figure 10.** Temperature curves of samples at (a) ablation center and (b) cool side under the same ablation conditions.

#### 4. Conclusions

The prepared  $C_{MP}/C$  composite has higher thermal conductivity in the X and Y directions. After the ablation test,  $CF_{PAN}$  becomes needle-shaped, while  $CF_{MP}$  shows a wedge shape. The fiber/matrix and matrix/matrix interfaces are preferentially oxidized and damaged during ablation. If there is no SiC coating, the  $C_{MP}/C$  and  $C_{PAN}/C$  composites show similar ablation rates during ablation. After being coated by SiC coating, thermal conductivity is believed to play a significant role in decreasing the hot-side temperature and protecting the coating from corrosion by the flame. The SiC-coated  $C_{MP}/C$  composite shows better ablation resistance than the SiC-coated  $C_{PAN}/C$  composite after a 120 s ablation test. The mass and linear ablation rates of the SiC-coated  $C_{MP}/C$  composite are only  $0.52 \mu\text{m}\cdot\text{s}^{-1}$  and  $0.19 \text{mg}\cdot\text{cm}^{-2}\cdot\text{s}^{-1}$ , respectively. The result indicates that the  $C_{MP}/C$  composite can effectively decrease the hot side temperature by rapidly conducting heat to the cool side, which can improve its ablation resistance.

This work is focused on the microstructural features and ablation properties of  $C_{MP}/C$  composite. Actually, the finite element model is believed to be an effective method to analyze its thermal conduction mechanism and ablation behavior. Further research on this advanced computational method is ongoing in this program.

**Author Contributions:** Conceptualization, D.H. and X.L.; Methodology, D.H. and B.L.; Validation, H.W., C.Y., P.Y. and J.Y.; Investigation, D.H. and C.Y.; Resources, X.L. and J.L.; Data Curation, D.H. and H.W.; Writing—Original Draft Preparation, D.H. and C.Y.; Writing—Review and Editing, D.H. and X.L.; Project Administration, X.L. and J.L.

**Funding:** This research was funded by The Innovation and Entrepreneurship Investment Project of Hunan Provincial Science and Technology Department (grant number: 2018GK5065), Research and Development Plan in Key Areas of Hunan Province (grant number: 2019GK2021), National Natural Science Foundation of China (grant number: 51372177, 51702094), and the Natural Science Foundation for Young Scientists of Hunan Province (2017JJ3014).

**Conflicts of Interest:** The authors declare no conflict of interest. The funders had no role in the design of the study; in the collection, analyses, or interpretation of data; in the writing of the manuscript, or in the decision to publish the results.

## Abbreviations

C/C composite	The carbon-fiber-reinforced carbon matrix (C/C) composite
CF	carbon fiber
PAN	polyacrylonitrile
CF <sub>PAN</sub>	PAN-based carbon fiber
CF <sub>MP</sub>	mesophase pitch-based carbon fiber
C <sub>MP</sub> /C composite	C/C composite prepared using the CF <sub>MP</sub> in the X (Y) direction and the CF <sub>PAN</sub> in the Z direction in this study
C <sub>PAN</sub> /C composite	C/C composite prepared using the CF <sub>PAN</sub> in all directions
CVI	chemical vapor infiltration
PIP	polymer infiltration and pyrolysis
CVR	chemical vapor reaction

## References

1. Sheehan, J.E.; Buesking, K.W.; Sullivan, B.J. Carbon-Carbon Composites. *Annu. Rev. Mater. Sci.* **1994**, *24*, 19–44. [[CrossRef](#)]
2. Fitzer, E. The future of carbon-carbon composites. *Carbon* **1987**, *25*, 163–190. [[CrossRef](#)]
3. Zhang, X.; Li, X.; Yuan, G.; Dong, Z.; Ma, G.; Rand, B. Large diameter pitch-based graphite fiber reinforced unidirectional carbon/carbon composites with high thermal conductivity densified by chemical vapor infiltration. *Carbon* **2017**, *114*, 59–69. [[CrossRef](#)]
4. Manocha, L.M.; Warriar, A.; Manocha, S.; Sathiyamoorthy, D.; Banerjee, S. Thermophysical properties of densified pitch based carbon/carbon materials—I. Unidirectional composites. *Carbon* **2006**, *44*, 480–487. [[CrossRef](#)]
5. Li, T.; Xu, Z.; Hu, Z.; Yang, X. Application of a high thermal conductive C/C composite in a heat-redistribution thermal protection system. *Carbon* **2010**, *48*, 924–925. [[CrossRef](#)]
6. Lachaud, J.; Aspa, Y.; Vignoles, G.L. Analytical modeling of the steady state ablation of a 3D C/C composite. *Int. J. Heat Mass Transf.* **2008**, *51*, 2614–2627. [[CrossRef](#)]
7. Lee, K.J.; Chen, Z.Y. Microstructure study of PAN–pitch-based carbon–carbon composite. *Mater. Chem. Phys.* **2003**, *82*, 428–434. [[CrossRef](#)]
8. Baxter, R.I.; Rawlings, R.D.; Iwashita, N.; Sawada, Y. Effect of chemical vapor infiltration on erosion and thermal properties of porous carbon/carbon composite thermal insulation. *Carbon* **1999**, *38*, 441–449. [[CrossRef](#)]
9. Kumar, S.; Kushwaha, J.; Mondal, S.; Kumar, A.; Jain, R.K.; Devi, R.G. Fabrication and ablation testing of 4D C/C composite at 10MW/m<sup>2</sup> heat flux under a plasma arc heater. *Mater. Sci. Eng. A* **2013**, *566*, 102–111. [[CrossRef](#)]
10. Levet, C.; Helber, B.; Couzi, J.; Mathiaud, J.; Gouriet, J.B.; Chazot, O.; Vignoles, G.L. Microstructure and gas-surface interaction studies of a 3D carbon/carbon composite in atmospheric entry plasma. *Carbon* **2017**, *114*, 84–97. [[CrossRef](#)]
11. Newcomb, B.A. Processing, structure, and properties of carbon fibers. *Compos. Part A Appl. Sci. Manuf.* **2016**, *91*, 262–282. [[CrossRef](#)]
12. Emmerich, F.G. Young’s modulus, thermal conductivity, electrical resistivity and coefficient of thermal expansion of mesophase pitch-based carbon fibers. *Carbon* **2014**, *79*, 274–293. [[CrossRef](#)]
13. Mochida, I.; Yoon, S.H.; Takano, N.; Fortin, F.; Korai, Y.; Yokogawa, K. Microstructure of mesophase pitch-based carbon fiber and its control. *Carbon* **1996**, *34*, 941–956. [[CrossRef](#)]
14. Wu, S.; Liu, Y.; Ge, Y.; Ran, L.; Peng, K.; Yi, M. Surface structures of PAN-based carbon fibers and their influences on the interface formation and mechanical properties of carbon-carbon composites. *Compos. Part A Appl. Sci. Manuf.* **2016**, *90*, 480–488. [[CrossRef](#)]
15. Paiva, M.C.; Bernardo, C.A.; Nardin, M. Mechanical, surface and interfacial characterisation of pitch and PAN-based carbon fibers. *Carbon* **2000**, *38*, 1323–1337. [[CrossRef](#)]
16. Qin, X.; Lu, Y.; Xiao, H.; Wen, Y.; Yu, T. A comparison of the effect of graphitization on microstructures and properties of polyacrylonitrile and mesophase pitch-based carbon fibers. *Carbon* **2012**, *50*, 4459–4469. [[CrossRef](#)]

17. Yuan, G.; Li, X.; Dong, Z.; Xiong, X.; Rand, B.; Cui, Z.; Cong, Y.; Zhang, J.; Li, Y.; Zhang, Z.; et al. Pitch-based ribbon-shaped carbon-fiber-reinforced one-dimensional carbon/carbon composites with ultrahigh thermal conductivity. *Carbon* **2014**, *68*, 413–425. [[CrossRef](#)]
18. Adams, P.M.; Katzman, H.A.; Rellick, G.S.; Stupian, G.W. Characterization of high thermal conductivity carbon fibers and a self-reinforced graphite panel. *Carbon* **1988**, *36*, 233–245. [[CrossRef](#)]
19. Luo, R.; Liu, T.; Li, J.; Zhang, H.; Chen, Z.; Tian, G. Thermophysical properties of carbon/carbon composites and physical mechanism of thermal expansion and thermal conductivity. *Carbon* **2004**, *42*, 2887–2895. [[CrossRef](#)]
20. Baxter, R.I.; Iwashita, N.; Sawada, Y. Effect of halogen purification and heat treatment on thermal conductivity of high porosity carbon/carbon composite thermal insulation. *J. Mater. Sci.* **2000**, *35*, 2749–2756. [[CrossRef](#)]
21. Klett, J.W.; Ervin, V.J.; Edie, D.D. Finite-element modeling of heat transfer in carbon/carbon composites. *Compos. Sci. Technol.* **1999**, *59*, 593–607. [[CrossRef](#)]
22. Ai, S.G.; He, R.J.; Pei, Y. M A numerical study on the thermal conductivity of 3d woven c/c composites at high temperature. *Appl. Compos. Mater.* **2015**, *22*, 823–835.
23. Li, K.; Shen, X.; Li, H.; Zhang, S.; Feng, T.; Zhang, L. Ablation of the carbon/carbon composite nozzle-throats in a small solid rocket motor. *Carbon* **2011**, *49*, 1208–1215. [[CrossRef](#)]
24. Li, H.; Yao, X.; Zhang, Y.; Li, K.; Guo, L.; Liu, L. Effect of heat flux on ablation behaviour and mechanism of C/C-ZrB<sub>2</sub>-SiC composite under oxyacetylene torch flame. *Corros. Sci.* **2013**, *74*, 265–270. [[CrossRef](#)]
25. Yoon, S.; Korai, Y.; Mochida, I. Crack formation in mesophase pitch-based carbon fibres: Part II Detailed structure of pitch-based carbon fibres with some types of open cracks. *J. Mater. Sci.* **1997**, *32*, 2759–2769. [[CrossRef](#)]
26. Li, C.Y.; Li, K.Z.; Li, H.J.; Ouyang, H.B.; Zhang, Y.L.; Guo, L.J. Ablation resistance and thermal conductivity of carbon/carbon composites containing hafnium carbide. *Corros. Sci.* **2013**, *75*, 169–175. [[CrossRef](#)]



© 2019 by the authors. Licensee MDPI, Basel, Switzerland. This article is an open access article distributed under the terms and conditions of the Creative Commons Attribution (CC BY) license (<http://creativecommons.org/licenses/by/4.0/>).